nature materials

SUPPLEMENTARY INFORMATION

https://doi.org/10.1038/s41563-018-0062-0

In the format provided by the authors and unedited.

# Motorizing fibres with geometric zero-energy modes

**Arthur Baumann[1], Antoni Sánchez-Ferrer[2], Leandro Jacomine[1], Philippe Martinoty[1], Vincent Le Houerou[1], Falko Ziebert[1,3]* and Igor M. Kulić[1]***

[1]Institut Charles Sadron UPR22-CNRS, Strasbourg Cedex 2, France. [2]Department of Health Sciences & Technology (D-HEST), Swiss Federal Institute of Technology (ETH Zürich), Zürich, Switzerland. [3]Institute for Theoretical Physics, Ruprecht-Karls-University, Heidelberg, Germany. *e-mail: f.ziebert@thphys.uni-heidelberg.de; kulic@unistra.fr

*Supplementary materials to*

# Motorizing fibres with geometric zero energy modes

Arthur Baumann, Antoni Sánchez-Ferrer, Leandro Jacomine,
Philippe Martinoty, Vincent Le Houerou, Falko Ziebert, Igor M. Kulic

## Supplementary video legends

**Supplementary Video 1 – Toroidal fiber motors**
**A nylon-6 ring** (fiber diameter 0.8 mm) rotating at plate temperature 180°C; video sped up 2-fold. **A PVDF ring** (fiber diameter 0.5 mm) rotating; video sped up 2-fold. **A PDMS ring** (fiber diameter 0.7 mm) rotating; video in real time.

**Supplementary Video 2 – Spiral fiber motor**
**Spiral fiber motor operation:** A 0.8 mm nylon-6 fiber wound as a spiral with 10 turns (outer diameter 14 cm) and held together with an aluminum holder, operated at 160°C. Marks on the fiber and the rotation of a fiber kink at one end indicate the rotation of the motor. Rubber tracers (red) placed on the fiber are transported by fiber rotation. Video is sped up 2-fold.
**Eiffel Tower lifting:** A 0.8 mm nylon-6 fiber wound as a spiral with 9.5 turns, operated at 180°C lifts a 20 g payload (a small brass copy of the Eiffel Tower). Video is sped up 5-fold.

**Supplementary Video 3: Self-propulsion of fibers**
**Spaghetti:** Uncooked dry spaghetti at 110°C. After the initial 'warm up', the sample runs also on a cold substrate, but in the opposite direction with respect to the curvature, until the substrate's and the fiber's temperatures have equilibrated. Video in real time.
**Silicone brush bristle:** A 1.5 mm mean diameter silicone rubber rod (slightly conical, cut from a baking brush), spinning on a 260°C hot plate. Sped-up 2-fold.
**PDMS rubber fiber:** diameter 0.7 mm, temperature 180°C. Sped-up 2-fold.
**Nylon fibers:** one nylon-6 fiber (diameter 0.6 mm) at 110°C, sped up 2-fold (cf. Video 4). Several nylon-6 fibers (diameter 0.5 mm) bouncing between two glass slides and mutually interacting; sped up 20-fold.

**Supplementary Video 4 – Annealing nylon-6 motors**
Two nylon-6 fibers (diameter 0.6 mm), one annealed at low temperature (110°C) and one at high temperature (180°C). Videos sped up 2-fold.

**Supplementary Video 5 – Fiber animation**
Dynamical evolution of an initially straight fiber on a hot plate. Temperature distribution in color code. The curvature is exaggerated for visualization purposes.

**Supplementary Video 6 – Ring self-healing**
A nylon-6 ring (fiber diameter 0.6 mm) of radius 3.2 cm rotating at plate temperature 195°C. A curvature defect appears and gradually self-heals. Video sped up 2-fold.

**Supplementary Video 7 – Thin filament loop**
A 120 $\mu$m diameter nylon-6 fiber loop (only one half of the loop is visible) spins at a mean frequency of 15 Hz. Video acquired at 320 fps and played at 30 fps.

# Supplementary methods

## Fiber motor preparation and testing

**Rings: annealing and dynamic self-healing.** Commercially available fishing line nylon-6 fibers ("Caperlan $4 \times 4$", supplier Decathlon, France) with diameters 600 or 800 $\mu$m were closed to rings of radii 2 to 6 cm via a small brass tube. The rings were gently annealed by raising the temperature beyond the onset of rolling over a course of few minutes, to relieve mechanical prestresses entrapped during the fabrication (extrusion) process. While linear open fibers are quite delicate to anneal (see below), closed rings displayed a robust and easy annealing process, probably due to their self-stabilizing shape. Compared to straight fibers, rings could be more easily directly exposed to larger temperatures than their onset temperature and they could be run robustly at slightly higher temperatures.
Interestingly, at elevated temperatures of 190-195°C rings could occasionally be seen to form localized strongly curved kink-like defects that however quickly reverted back to uniform curvature during a continuous operation (i.e. turning) of the ring, cf. Supplementary Fig. 1 and Supplementary Video 6. Very rarely at 190-195°C rings suffered an irreversible damage that led to a blocking of their rotation without any visible kink or obvious defect. Nevertheless, the majority of the rings stayed functional and rotating for days.

**Spirals: annealing and long time testing of the spiral motor.** Compared to the ring motors, spiral fiber motors (made from nylon-6) that were held in shape by a aluminum holder had to be annealed more carefully and slowly due to frictional interactions with the holder. The holder-fiber interactions lead to an occasional undesired pinning of the thermally shortening fiber onto the holder. The latter process could be prevented by a slower first annealing cycle (gentle raising temperature in 10-15 minutes from 100-160°C) and occasional gentle stirring of the fiber (with a silicone brush) along its tangents to relieve built-up strains and to unpin from the holder.
A long time testing, cf. Supplementary Fig. 2, of annealed spiral motors reveals a continuous operation of the device with a gradual decay of turning speed on a timescale of tens of hours. Data have been obtained from a nylon-6 spiral (600 $\mu$m diameter, 3.2 m total length) running at an operating temperature of $T = 160$°C; the spiral was observed to operate continuously for 24 hours loosing approximately half of its initial angular velocity in this time period.

**Linear fiber motors.**
**Nylon-6 fibers** with diameters ranging from 800 down to 120 $\mu$m were gently annealed by slowly heating the fiber on the heating plate from their onset temperature of rolling (for $600 - 800\,\mu$m fibers 100-110°C) up to their optimal running temperatures 180-185°C. In a typical annealing procedure, the temperatures were gently raised over a course of several minutes so that the fiber gradually liberates defects and prestresses via the process of combined heating and their spontaneous rolling, cf. Supplementary Fig. 3. All fibers that were subjected to even a single training run could in the following runs be directly exposed to the highest operation temperatures without damage and were immediately engaging in the rolling process (see also Fig. 5B in the main manuscript). This memory effect of the first training run could be observed within a long period of up to several days after the training.
Skipping the first gradual training run and instead directly exposing the fibers to temperatures higher than their onset temperature (of 140°C-180°C) resulted in a rapid reshaping of the fiber and catastrophic deformations, see Supplementary Fig. 4, despite the fact that the process happens far below the melting temperature ($T_{melt} = 215$°C). This uncontrolled exposure process led in most cases to very poorly mobile or completely immobile fibers. The final torturously deformed irregular fiber shape

was irreversible and could not be reverted even up to the point of fiber melting. These tests underline the importance of a first gentle training run for reproducible rotation of linear, open fibers.
The annealing of thinner nylon-6 fibers, below 0.2 mm in radius, becomes increasingly delicate and structural defects (like bends, kinks and twisted helical sections) appear more often. Consequently, a reproducible annealing process of thinner samples requires a slower annealing procedure in comparison to thicker fibers. For consistency reasons, all nylon-6 fibers used for angular velocity measurements were annealed according to the same minimal protocol: Starting from 100°C the temperature is raised to 160°C at a heating rate of 15 K/min followed by a gentler increase from 160°C to the highest temperature of 185°C at 7 K/min. Following this protocol leads to close to 100% functional fiber motor samples for all probed thicknesses.

For the **PVDF fiber samples** ("Phen-X-Fluorocarbone" fishing line fibers, supplier Decathlon, France; diameter 0.5 mm) the annealing is more delicate than for nylon-6. A modified annealing protocol respecting the lower PVDF melting temperature ($T_m = 177$°C) was followed, with a temperature raise from 130°C up to 170°C at a slower heating rate of 1K/min. After annealing PVDF fibers move with comparable velocities as their nylon-6 counterparts, see Supplementary Fig. 5 in comparison to Fig. 5B in the main manuscript.

The **PDMS fiber samples** were prepared in house in the way described in the materials section and did not need any annealing.

In addition to quantitiative studies on nylon-6 and PVDF fishing lines, we also made qualitative tests using starch (commerical, dry spaghetti) and silicone fibers (bristles cut from a commercial cooking brush). Both – amorphous – fibers also displayed the rolling motion, cf. Supplementary Fig. 6. In addition, Supplementary Fig. 6C exemplifies a collective motion of several nylon fibers confined between two glass cover slips.

**Effect of fiber length on stability:** The length of the linear fiber plays a certain role in their ability to roll smoothly and reproducibly. Occasionally, especially at temperatures only slightly above the onset of rolling motion, short PVDF and nylon-6 fibers (i.e. less than 5 cm in length) became stuck in a metastable out-of-plane deformed position. They stayed suspended above the plate by only two contact points (their two ends) for several seconds, leading to intermittent motion and more frequent direction reversal. To avoid this behavior only longer fiber samples ($> 8$ cm) running sufficiently smoothly were used for quantitative measurements.

## Linear and angular velocities

Linear velocities were measured by tracing the fibers' positions from time-lapse and high speed recordings. The angular velocities were extracted by tracing color marks painted on fibers from high speed recordings of the rolling process on a Phantom MIRO LC 320S camera.
The comparison of the linear and angular velocities of single fibers with a given radius $R$ revealed measurable differences between the expected angular velocities $\omega_e = v/R$ and the directly measured $\omega_m$ with $\omega_m$ being consistently smaller than $\omega_e$. This effect is especially pronounced for very thin fibers with the ratio $\omega_e/\omega_m$ approaching 2 for the thinnest samples. The discrepancy is resolved by carefully observing the dynamical shape evolution of the fibers. During the rolling process, the fibers seem to slightly but visibly fluctuate in shape in a periodic manner. This observation together with $\omega_e/\omega_m$ different from unity implies that the fiber shape is slightly deviating from ideal and displays

small amplitude, large wavelength bends. When rotating the bend defects give rise to an increase of the effective fiber diameter beyond the nominal fiber thickness. The ratio between the nominal and effective radius of fibers of different thickness is depicted in Supplementary Fig. 7.

## Mechanical characterization of nylon fibers

Dynamic mechanical thermal analysis (DMTA) tests were carried out with an Instron E3000 dynamic tensile machine. Cylindrical filament samples of nylon-6 of 0.8 mm diameter were clamped into the sample holder. The temperature was varied from 30 to 190°C in steps of 20°C. During the DMTA tests, twenty-seven logarithmically spaced sinusoidal waves were employed at frequencies between 0.1 and 8.93 Hz. A strain control was used during tests with minimum and maximum strain levels of $3 \cdot 10^{-3}$ and $5 \cdot 10^{-3}$, respectively.
Supplementary Fig. 8 shows the storage modulus, $E'$, and the loss modulus, $E''$, for the used nylon-6 as a function of frequency for different temperatures. In the relevant temperature range for the elasto-rotation experiments (130-190°C), both moduli are almost frequency-independent, implying a constant loss tangent.

## Structural characterization of nylon fibers

In order to analyze the structural features of the fibers, their crystallinity and anisotropy, wide-angle X-ray scattering (WAXS) experiments were performed using a Rigaku S-MAX3000 equipped with a Rigaku MicroMax-007HF copper rotating anode generator (12 kW, 40 kV, 300 mA) with radiation of wavelength $\lambda_{\mathrm{CuK}\alpha} = 0.15418$ nm. The scattering intensities were collected by a Fujifilm BAS-MS 2025 imaging plate system (20 cm × 25 cm, 50 $\mu$m resolution) and a 2D Triton-200 X-ray gas-filled multi-wire detector (120 mm diameter, 100 $\mu$m resolution). An effective scattering vector range of 0.1 $\mathrm{nm}^{-1} < q < 25\ \mathrm{nm}^{-1}$ was obtained, where $q$ is the scattering wave vector defined as $q = 4\pi \sin\theta/\lambda_{\mathrm{CuK}\alpha}$ with a scattering angle of $2\theta$. Samples were placed in a self-constructed holder controlled by a Haake-F3 thermostat.
The 2D WAXS intensity profile of the annealed nylon-6 fiber shows the semicrystalline and anisotropic pattern of the sample at 120 and 185°C (Supplementary Fig. 9a and b, respectively), while isotropic and amorphous at 240°C due to the melting of the sample as visualized by the isotropic halo in Supplementary Fig. 9c. At 120°C, the sample presents two equatorial (red section), two meridional (green section), and one reflection at 45 degrees (blue section). The same sample at 185°C only shows one equatorial reflection (red section), two meridional (green section), and one reflection at 45 degrees (blue section). At temperatures above 220°C, nylon-6 melts and scatters isotropically.
Nylon-6 is a semicrystalline polymer with a degree of crystallinity of $\chi = 40 - 50\%$ and has three thermal transitions: a second-order transition corresponding to the glass transition of the amorphous domains at $T_g \simeq 50$°C, and two first-order transitions attributed to an order-to-order transition of the crystals within the sample at $T_{\alpha\gamma} = 175 - 195$°C and to the melting of the crystalline domains at $T_m = 210 - 220$°C, respectively [31].
In Supplementary Fig. 10, the 1D WAXS intensity profile for the annealed nylon-6 fiber at 120, 185, and 240°C is shown. The sample has different sets of peaks at the three temperatures, i.e., $q(120°\mathrm{C}) = 7.2$, 9.7, 13.5, 14.5, 16.0, 19.1 $\mathrm{nm}^{-1}$, $q(180°\mathrm{C}) = 7.4$, 9.7, 13.2, 15.0, 18.8 $\mathrm{nm}^{-1}$, and $q(240°\mathrm{C}) = 8.8$, 13.5, 17.9 $\mathrm{nm}^{-1}$. At 120°C, the two equatorial peaks at $q = 14.5$ and 16.0 $\mathrm{nm}^{-1}$ merge together into a single peak at $q = 15.0\ \mathrm{nm}^{-1}$ when heated at 185°C, and this peak vanishes when the sample is a melt at 240°C. This change in the WAXS pattern from 120 to 185°C is attributed to a polymorphic transformation from the $\alpha$-phase to the $\gamma$-phase of nylon-6 [32].
The $\alpha$-polymorphism of nylon-6 [33] corresponds to the monoclinic system ($a = 4.82$Å, $b = 4.28$Å, $c = 17.45$Å, $\gamma = 62.50°$) [34] with the polymer chains interacting in an antiparallel fashion by means

of hydrogen bonds [35]. Thus, the average lateral distances between the nylon-6 chains is $d = 4.55$Å, while the length of the repeat unit in the polymer backbone is $l = 8.72$Å ($q = 7.2$ nm$^{-1}$). The $\gamma$-polymorphism of nylon-6 [33] belongs to the orthorhombic system ($a = 4.86$Å, $b = 4.59$Å, $c = 16.98$Å, $\gamma = 60.38°$), where the interchain average distance is $d = 4.72$Å and the repeat unit length decreases to a value of $l = 8.49$Å ($q = 7.4$ nm$^{-1}$). At temperatures above the melting point, e.g., 240°, nylon-6 has an average polymer-polymer distance of $d = 4.66$Å.
From the values of the lattice parameters for each polymorphism, both the linear thermal expansion coefficient along the fiber axis, $\alpha_\parallel$, and in the cross-section of the fiber, $\alpha_\perp$, were calculated. Nylon-6 has a positive value for $\alpha_\perp = 4.5 \cdot 10^{-4}\mathrm{K}^{-1}$ (expansion factor $1.92 \cdot 10^{-3}$ÅK$^{-1}$ and corresponding thermal strain 2.92%) from 120 to 185°C and a negative value for $\alpha_\parallel = -4.1 \cdot 10^{-4}\mathrm{K}^{-1}$ ($-7.20 \cdot 10^{-3}$ÅK$^{-1}$ and $-2.68$%) from 120 to 185°C. Thus, nylon-6 fibers expand radially while contract longitudinally with an estimated volumetric expansion of $V = 3.03 \cdot 10^{-1}$Å$^3$K$^{-1}$ ($4.8 \cdot 10^{-4}$K$^{-1}$ or 3.09%).
Accounting for the fact that the degree of crystallinity is $\chi = 46 - 48$%, cf. Supplementary Fig. 10, this amounts to an effective thermal expansion coefficient of the nylon-6 fibers along the fiber axis of $\alpha_\parallel = -1.93 \cdot 10^{-4}\mathrm{K}^{-1}$ and a corresponding strain $\Delta\varepsilon = -1.26$%. To cross check this value, derived from structural data, we measured the longitudinal strain directly (by video analysis of the fiber's contour length) from rolling fiber experiments, cf. Supplementary Fig. 11. In the temperature range from 120 to 180°C, the total strain is about $\Delta\varepsilon = -1.5$%, in rather good agreement with the one found from structural data. Note, however, that the strain (and hence thermal expansion) deviates from linearity.

## Theoretical description

In the following we briefly describe our theoretical considerations. First, we show how temperature gradients in the cross-section of the fiber lead to torque creation if the symmetry is broken (i.e. a zero elastic energy mode exists) by the presence of an in-plane fiber curvature. We also discuss self-induced fiber curving and the balance of the acting torques. Starting from the thermal diffusion equation with angular advection, we then derive dynamic equations for the temperature gradients. This completes the reduced description, summarized by three equations: the torque balance and two equations for the thermal gradients/strains in-plane and normal to the plane, as already given in the main manuscript. We then investigate the stationary rotating solutions of these equations, both for a fiber closed into a circle and for a straight fiber. Finally, we describe a simple description of the torque creation and energy storage of a fiber forced into a spiral path, cf. Fig. 3 in the main manuscript.

## Torque creation, torque balance and thermally induced curvature

Let the heating plate define the $X$-$Y$-plane. When considering a cross-section of the fiber, without restriction we can lay the fiber axis along $Y$. The fiber's (vectorial) curvature is then along $X$, $\vec{\kappa} \cdot e_x = \kappa_x = \kappa$. This defines the lab frame.
The angle $\Phi$ (with respect to the $X$-axis, cf. Supplementary Fig. 12) describes a rotation of the fiber's cross-section along its axis (i.e. along the $Y$-axis) and introduces the co-rotating/internal coordinate system

$$e_1 = (\cos\Phi, \sin\Phi)\,, \quad e_2 = (-\sin\Phi, \cos\Phi) \qquad \text{(Supp. Eq.1)}$$

with the internal coordinates $(X', Z')$ or in polar form $(\rho, \phi)$. In these internal coordinates, the *axial*

*strain in the cross-section* (corresponding to the strain tensor component $\epsilon_{YY}$) can be written as

$$\epsilon(\rho,\phi) = -\rho(\kappa_1\cos\phi + \kappa_2\sin\phi) + \bar{\epsilon} - \epsilon_T(\rho,\phi)\,. \qquad \text{(Supp. Eq.2)}$$

The first contribution is due to bending, where the negative sign indicates compression within the cross-section at the inwards curved side. $\bar{\epsilon}$ is the strain related to axial compression/elongation and $\epsilon_T(\rho,\phi)$ is the thermal prestrain due to axial thermal expansion/shortening. We can express the strain solely via the curvature in the lab frame $\kappa$, using $\kappa_1 = \vec{\kappa}\cdot e_1 = \kappa\cos\Phi\,,\ \ \kappa_2 = \vec{\kappa}\cdot e_2 = -\kappa\sin\Phi$, to get

$$\epsilon(\rho,\phi) = -\rho\kappa\cos(\phi+\Phi) + \bar{\epsilon} - \epsilon_T(\rho,\phi)\,. \qquad \text{(Supp. Eq.3)}$$

The elastic energy (of the cross-section, i.e. energy per length for the fiber) then reads

$$\begin{aligned} E(\kappa,\bar{\epsilon},\Phi) &= \frac{Y}{2}\int\left(-\rho\kappa\cos(\phi+\Phi) + \bar{\epsilon} - \epsilon_T(\rho,\phi)\right)^2\rho d\rho d\phi \\ &= \frac{1}{2}B\kappa^2 + \frac{Y}{2}\int\left(\bar{\epsilon} - \epsilon_T(\rho,\phi)\right)^2\rho d\rho d\phi + Y\kappa\int\cos(\phi+\Phi)\epsilon_T(\rho,\phi)\,\rho^2 d\rho d\phi \end{aligned} \qquad \text{(Supp. Eq.4)}$$

where $Y$ is Young's modulus and $B = \frac{\pi}{4}YR^4$ is the bending stiffness.
The thermal axial prestrain is given by

$$\epsilon_T(\rho,\phi) = \alpha_\parallel\Delta T(\rho,\phi)\,, \qquad \text{(Supp. Eq.5)}$$

with $\alpha_\parallel$ the linear thermal expansion coefficient along the fiber axis. Note that in writing this we have neglected shear in the cross-section, torsional contributions etc. For the temperature distribution we make the following ansatz,

$$\Delta T(\rho,\phi) = \Delta T_c\frac{\rho}{R}\cos\phi + \Delta T_s\frac{\rho}{R}\sin\phi + \Delta T_0\,, \qquad \text{(Supp. Eq.6)}$$

introducing the two principal temperature differences ('modes') $\Delta T_c$ and $\Delta T_s$, in the rotating frame, as well as a homogeneous offset $\Delta T_0$. Minimization of (Supp. Eq.4) w.r.t. $\bar{\epsilon}$ yields a relation between the compressive/elongational and the thermal strain

$$\bar{\epsilon} = \frac{1}{\pi R^2}\int\epsilon_T(\rho,\phi)\rho d\rho d\phi\,, \qquad \text{(Supp. Eq.7)}$$

which upon insertion of (Supp. Eq.6) yields $\bar{\epsilon} = \alpha_\parallel\Delta T_0$, i.e. the homogeneous part of the thermal stress is compensated. Insertion into the energy and performing all integrals yields

$$E(\kappa,\Phi) = B\left\{\frac{1}{2}\kappa^2 + \alpha_\parallel\frac{\kappa}{R}(\Delta T_c\cos\Phi - \Delta T_s\sin\Phi) + \frac{\alpha_\parallel^2}{2R^2}(\Delta T_c^2 + \Delta T_s^2)\right\}\,, \qquad \text{(Supp. Eq.8)}$$

where the last term has no consequence for the dynamics (of $\kappa$ and $\Phi$).

The **driving torque**, generating the rolling motion if it overcomes the prevalent dissipation mechanisms, is hence given by $m = -\frac{\partial E}{\partial\Phi}$, implying

$$m = B\alpha_\parallel\frac{\kappa}{R}(\Delta T_c\sin\Phi + \Delta T_s\cos\Phi)\,, \qquad \text{(Supp. Eq.9)}$$

where $\kappa = \kappa_{\text{ext}} = \frac{1}{R_{\text{ext}}}$ is the – externally imposed – curvature of the ring.

In case of an initially straight, linear, open fiber, (Supp. Eq.8) also yields the **thermally induced curvature**. Namely, the curvature entering the driving torque is the stationary curvature $\kappa_s$ – neglecting initial, transient reshaping events of the linear fiber – that can be obtained via minimization, $0 = -\frac{\partial E}{\partial \kappa}$, yielding

$$\begin{aligned} 0 &= B\left(-\kappa - \frac{\alpha_\parallel}{R}(\Delta T_c \cos\Phi - \Delta T_s \sin\Phi)\right) \\ \rightarrow\ \kappa_s &= -\frac{\alpha_\parallel}{R}(\Delta T_c \cos\Phi - \Delta T_s \sin\Phi)\,. \end{aligned} \qquad \text{(Supp. Eq.10)}$$

We can simplify these results by transforming back to the lab frame. In fact, since

$$\begin{pmatrix} X' \\ Z' \end{pmatrix} = \begin{pmatrix} \cos\Phi & \sin\Phi \\ -\sin\Phi & \cos\Phi \end{pmatrix} \begin{pmatrix} X \\ Z \end{pmatrix} \qquad \text{(Supp. Eq.11)}$$

we can rewrite (Supp. Eq.6) as

$$\begin{aligned} \Delta T(\rho,\phi) - \Delta T_0 &= (\Delta T_c \cos\Phi - \Delta T_s \sin\Phi)\frac{X}{R} + (\Delta T_c \sin\Phi + \Delta T_s \cos\Phi)\frac{Z}{R} \\ &= \Delta T_x \frac{X}{R} + \Delta T_z \frac{Z}{R}\,, \end{aligned} \qquad \text{(Supp. Eq.12)}$$

identifying the two principal temperature differences ('modes') $\Delta T_x$ and $\Delta T_z$ in the lab frame. Introducing the thermal strain differences

$$x = \alpha_\parallel \Delta T_x\,, \ \text{ and } \ z = \alpha_\parallel \Delta T_z\,, \qquad \text{(Supp. Eq.13)}$$

the driving torque and the stationary thermally-induced curvature hence read

$$\begin{aligned} m &= B\frac{\kappa}{R}\alpha_\parallel \Delta T_z = \frac{\pi}{4} Y R^3 \kappa z\,, \\ \kappa_s &= -\frac{\alpha_\parallel \Delta T_x}{R} = -\frac{x}{R}\,, \end{aligned} \qquad \text{(Supp. Eq.14)}$$

as given in the main manuscript.

**Torque balance.** To write down the balance of torques, we also have to account for the dominant dissipation mechanisms.
In case of a *closed fiber ring* – forced into a circle of radius $R_{\rm ext}$ – one has the typical strain $\epsilon \simeq \kappa_{\rm ext} R = R/R_{\rm ext} \simeq \frac{0.2\text{mm}}{2\text{cm}} = 10^{-2}$. Our mechanical characterization of nylon-6, Supplementary Fig. 8, implies in the relevant temperature range a storage modulus of $E' = Y = 500 - 800$ MPa and a loss modulus of $E'' = 10 - 30$ MPa. Hence the stress induced by the externally imposed curvature is of order $\sigma = E'\epsilon \simeq 5 - 8$ MPa, comparable to the loss modulus, and internal (viscoelastic) dissipation is important. The associated dissipative torque can be estimated to be of order $m_{\rm dissip} = E''(|\kappa_{\rm ext}|R)R^2$, with $E''$ the loss modulus, $\kappa_{\rm ext} R$ the strain (wherein for dissipation the sign of the curvature does not matter) and an additional factor $R^2$ stemming from the cross-section. Note that in the relevant temperature range, $E''$ and hence the dissipation is independent of (angular) velocity, cf. Supplementary Fig. 8.
In contrast, in the case of an initially *straight filament*, the thermally induced curving strain, cf. (Supp. Eq.14), is very small: $\epsilon \simeq \kappa R = x = \alpha_\parallel \Delta T_x \simeq 10^{-4}$. Hence dissipation in the material due to curving is negligible and rolling friction is the dominating dissipation mechanism. The dissipative torque due to rolling friction is given by $m_{\rm fric} = C_r \pi R^2 \bar{\rho} g R$, where $C_r$ is the coefficient of rolling

friction, $\pi R^2 \bar{\rho} g$ is the gravitational normal force per length (with $\bar{\rho}$ the density and $g$ the gravitational acceleration) and $R$ is the lever arm. Note that – again – dissipation is independent of (angular) velocity.
Including the driving torque given in (Supp. Eq.14) and a possible external torque $m_{\text{ext}}$, the general torque balance given in the main text,

$$m = m_{\text{fric}} - m_{\text{ext}} \,, \tag{Supp. Eq.15}$$

can be specified to

$$\frac{\pi}{4} Y R^3 \kappa_{\text{ext}} z = E'' |\kappa_{ext}| R^3 - m_{\text{ext}} \tag{Supp. Eq.16}$$

for a closed filament, i.e. a ring, and to

$$\frac{\pi}{4} Y R^3 \kappa_s z = C_r \bar{\rho} g \pi R^3 - m_{\text{ext}} \tag{Supp. Eq.17}$$

in case of an initially straight filament. In the case where rolling is absent, obviously the dissipative contributions on the r.h.s. of (Supp. Eq.17) and (Supp. Eq.16) vanish.
It is interesting to note that – in the absence of external torques – in both cases the dependence on the cross-section radius cancels. The main difference, which will be important later on for the dynamics, is that for the ring the curvature is slaved by the externally imposed curvature $\kappa_{\text{ext}} = \frac{1}{R_{\text{ext}}}$, while for the straight filament the thermally-induced curvature $\kappa_s$ is 'self-organized'.

## Dynamics of the temperature distribution

To close the description, dynamic equations for the thermal strain differences as defined in (Supp. Eq.13), i.e. for the principal temperature differences ('modes') $\Delta T_x$, $\Delta T_z$ are needed. They can be derived from the thermal diffusion equation for the cross-section that is turning with – in the stationary case constant – angular frequency $\omega$,

$$\partial_t T = \frac{D}{R^2} \nabla^2 T + \omega \partial_\varphi T \,. \tag{Supp. Eq.18}$$

This equation is in the lab frame [with $(r, \varphi)$ the respective polar coordinates, with $\varphi = 0$ at the contact with the plate, i.e. $\varphi$ is the angle with respect to the $-Z$-axis] and we have scaled length by the cross-section's radius $R$, hence $r \in [0, 1]$. $D$ is the thermal diffusivity of the polymeric material, given by the ratio of thermal conductivity over the specific heat per unit volume, $D = \frac{k_{\text{pol}}}{C_{\text{pol}}}$.
(Supp. Eq.18) has to be considered with the following boundary condition:

$$\frac{l(\varphi)}{R} \partial_r T + (T - T_{\text{ext}}(\varphi)) = 0 \quad \text{at} \quad r = 1 \,, \tag{Supp. Eq.19}$$

where $l(\varphi)$ is a thermal length scale, given by the ratio of the thermal conductivity of the material and the heat transfer coefficient, and $T_{\text{ext}}(\varphi)$ is the externally imposed temperature.
At the bottom (contact to the heating plate) we assume $T_{\text{ext}} = T_s$ and $l(\varphi = 0) = 0$, implying perfect thermal contact.
At the top (contact to air), heat transfer to a fluid has to be accounted for, and one has $T_{\text{ext}} = T_{\text{air}}$ and $l(\varphi = \pi) = l_{\text{th}} = \frac{k_{\text{pol}}}{h}$, where $h = \frac{k_{\text{air}}}{d} f(Ra, Pr)$ scales with the diameter $d = 2R$ of the fiber in a complicated fashion involving the Rayleigh number $Ra(d)$ (and Prandtl number $Pr$) – already for a stationary, non-rotating cylinder. We estimated that in the considered system $l_{\text{th}} \simeq R$.

To capture the main physics, we will need only the dominant modes of the temperature distribution. Therefore we can assume a symmetry adapted version of the boundary conditions (at $r = 1$):

$$l(\varphi) = (1 - \cos\varphi)\frac{l_{\text{th}}}{2}\,, \tag{Supp. Eq.20}$$

$$T_{\text{ext}}(\varphi) = \frac{T_s - T_{\text{air}}}{2}\cos\varphi + \frac{T_s + T_{\text{air}}}{2}\,, \tag{Supp. Eq.21}$$

Like that, one indeed has $l = 0$ and $T = T_s$ at the bottom ($\varphi = 0$) and $l = l_{\text{th}}$ and $T_{\text{air}}$ at the top ($\varphi = \pi$). For brevity we introduce $T_{\text{ext}}(\varphi) = T^- \cos\varphi + T^+$, where $2T^- = T_s - T_{\text{air}} = \Delta T_{\text{ext}}$ is the externally applied temperature difference.
As discussed in the last section, we are looking for a solution of the form

$$T = C(r)\cos\varphi + S(r)\sin\varphi + T_0\,. \tag{Supp. Eq.22}$$

To proceed, it is convenient to use a symmetry-adapted polynomial system, namely Zernike-polynomials, which are defined [36] as

$$Z_n^m = R_n^m(r)\cos(m\varphi)\,,\quad Z_n^{-m} = R_n^m(r)\sin(m\varphi) \tag{Supp. Eq.23}$$

with the radial polynomials $R_n^m$, or explicitly as

$$Z_0^0 = 1\,, \tag{Supp. Eq.24}$$

$$Z_1^1 = 2r\cos\varphi\,,\quad Z_1^{-1} = 2r\sin\varphi\,, \tag{Supp. Eq.25}$$

$$Z_3^1 = \sqrt{8}(3r^3 - 2r)\cos\varphi\,,\quad Z_3^{-1} = \sqrt{8}(3r^3 - 2r)\sin\varphi\,. \tag{Supp. Eq.26}$$

Note the following properties of the Zernike polynomials (with $\nabla^2$ the Laplacian):

$$\nabla^2 Z_0^0 = 0\,,\quad \nabla^2 Z_1^{\pm 1} = 0\,,\quad \nabla^2 Z_3^{\pm 1} = 24 Z_1^1. \tag{Supp. Eq.27}$$

By inspection of the ansatz, (Supp. Eq.22), one could think that it is sufficient to use only the modes $\propto Z_1^{\pm 1}$. However, to be able to fulfill the boundary conditions, one also needs to account for $\propto Z_3^{\pm 1}$. We hence write

$$C(r)\cos\varphi = c_1 Z_1^1 + c_2 Z_3^1\,,\quad S(r)\sin\varphi = s_1 Z_1^{-1} + s_2 Z_3^{-1}\,. \tag{Supp. Eq.28}$$

Insertion of this ansatz into the boundary condition, (Supp. Eq.20), using $\cos\varphi\sin\varphi = \frac{1}{2}\sin(2\varphi)$ and $\cos^2\varphi = \frac{1}{2}(1 + \cos(2\varphi))$, sorting for modes and neglecting modes $m \geq 2$ yields three equations for the unknowns $c_2$, $s_2$, $T_0$:

$$0 = \frac{l_{\text{th}}}{2R}C'(1) + (C(1) - T^-)\,, \tag{Supp. Eq.29}$$

$$0 = \frac{l_{\text{th}}}{2R}S'(1) + S(1) \tag{Supp. Eq.30}$$

$$0 = -\frac{l_{\text{th}}}{4R}C'(1) + T_0 - T^+\,. \tag{Supp. Eq.31}$$

(Supp. Eq.31) yields

$$T_0 = \frac{l_{\text{th}}}{4R}C'(1) + T^+\,. \tag{Supp. Eq.32}$$

(Supp. Eq.30) relates $s_2$ to $s_1$, and hence implies that the mode $\propto Z_3^{-1}$ is slaved to the mode $\propto Z_1^{-1}$,

$$s_2 = -g s_1 \quad \text{with } g = \frac{2\left(\frac{l_{\text{th}}}{R}+2\right)}{\sqrt{8}\left(7\frac{l_{\text{th}}}{R}+2\right)} \tag{Supp. Eq.33}$$

and the coupling constant $g$ depending on the two length scales of the system, the fiber radius $R$ and the thermal length $l_{\text{th}}$. Similarly from (Supp. Eq.29):

$$c_2 = g(c_{\text{stat}} - c_1) \quad \text{with } c_{\text{stat}} = \frac{T^-}{\frac{l_{\text{th}}}{R}+2} = \frac{\Delta T_{\text{ext}}}{2\left(\frac{l_{\text{th}}}{R}+2\right)}\,. \tag{Supp. Eq.34}$$

We will see shortly that $c_{\text{stat}}$, which is proportional to the thermal drive, describes the stationary temperature distribution.
Now we insert the ansatz, (Supp. Eq.22) and (Supp. Eq.28), with $c_2$, $s_2$, $T_0$ from above into the thermal diffusion equation, (Supp. Eq.18). We then project on the mode $Z_1^{-1}$ by performing $\int_0^1 ... Z_1^{-1} r\, dr$ of the resulting equation, and analogously we project on $Z_1^1$, to get equations for $s_1$ and $c_1$ as follows:

$$\dot{s}_1 = -\frac{24D}{R^2} g s_1 - \omega c_1\,, \tag{Supp. Eq.35}$$

$$\dot{c}_1 = -\frac{24D}{R^2} g c_1 + \frac{24D}{R^2} g c_{\text{stat}} + \omega s_1\,. \tag{Supp. Eq.36}$$

Inspecting the ansatz (Supp. Eq.22) and the definition of $\varphi$, $c_1$ corresponds to $\Delta T_z$ and $s_1$ to $\Delta T_x$ and we can hence write the dynamics of the temperature field in the following simple form:

$$\frac{d}{dt}\Delta T_x = -\frac{\Delta T_x}{\tau} - \omega \Delta T_z\,, \tag{Supp. Eq.37}$$

$$\frac{d}{dt}\Delta T_z = q - \frac{\Delta T_z}{\tau} + \omega \Delta T_x\,. \tag{Supp. Eq.38}$$

Here $\tau$ is the characteristic time scale of thermal relaxation. The mode $\Delta T_z$ is in addition driven by the thermal pumping, with $q$ the pumping rate. Explicitly we get

$$\tau = \frac{R^2}{24Dg} = \frac{R^2}{24D}\frac{\sqrt{8}\left(7\frac{l_{\text{th}}}{R}+2\right)}{2\left(\frac{l_{\text{th}}}{R}+2\right)}\,, \tag{Supp. Eq.39}$$

$$q = \frac{24D}{R^2} g c_{\text{stat}} = \frac{24D}{R^2}\frac{\Delta T_{\text{ext}}}{\sqrt{8}\left(7\frac{l_{\text{th}}}{R}+2\right)}\,. \tag{Supp. Eq.40}$$

If we consider (Supp. Eq.37) and (Supp. Eq.38) for the case without rotation ($\omega = 0$), one gets for long times $\Delta T_x = 0$ and $\Delta T_z = q\tau = c_{\text{stat}} = \frac{\Delta T_{\text{ext}}}{2\left(\frac{l_{\text{th}}}{R}+2\right)}$, which is the expected solution in this case.

To sum it up, introducing the thermal strains $x = \alpha_\parallel \Delta T_x$ and $z = \alpha_\parallel \Delta T_z$, and the effective thermal drive $p = \alpha_\parallel q$ we arrive at the equations given in the main text:

$$\dot{x} = -\frac{x}{\tau} - \omega z\,, \tag{Supp. Eq.41}$$

$$\dot{z} = p - \frac{z}{\tau} + \omega x\,. \tag{Supp. Eq.42}$$

Together with the torque balance, in case of a rotating circular fiber given by (Supp. Eq.16),

$$\frac{\pi}{4} Y R^3 \kappa_{\rm ext} z = E'' |\kappa_{\rm ext}| R^3 - m_{\rm ext} \qquad \text{(Supp. Eq.43)}$$

and in case of a rolling straight fiber, (Supp. Eq.17) with $\kappa_s$ given by (Supp. Eq.14),

$$\frac{\pi}{4} Y R^3 \kappa_s z = C_r \bar{\rho} g \pi R^3 - m_{\rm ext} \ , \quad \kappa_s = -\frac{x}{R} \qquad \text{(Supp. Eq.44)}$$

the dynamics is now completely determined.

### Onset of motion: prescribed curvature (circle, spiral) vs. straight fiber

**Fiber closed to a circle.** In this case, one looks for solutions to the steady-state equations

$$\frac{\pi}{4} Y R^3 \frac{z}{R_{\rm ext}} = m_{\rm dissip}(\omega) - m_{\rm ext} \,, \qquad \text{(Supp. Eq.45)}$$

$$0 = -\frac{x}{\tau} - \omega z \,, \qquad \text{(Supp. Eq.46)}$$

$$0 = p - \frac{z}{\tau} + \omega x \,. \qquad \text{(Supp. Eq.47)}$$

where we inserted the externally prescribed curvature $\kappa_{\rm ext} = 1/R_{\rm ext}$ and where the dissipative torque is given by $m_{\rm dissip}(\omega = 0) = 0$ and $m_{\rm dissip}(\omega \neq 0) = \frac{E'' R^3}{R_{\rm ext}}$ for internal viscoelastic dissipation. The trivial solution (for $m_{\rm ext} = 0$) is given by $\omega = 0$, $x = 0$ and $z = p\tau$; note that the l.h.s. of the torque balance is finite, i.e. a fiber closed to a ring is under prestrain.
For $m_{\rm ext} = 0$, one gets from the torque balance a stationary value for the strain difference normal to the plane, $z_s = \frac{4}{\pi} \frac{E''}{Y}$, which mainly is the ratio of the loss vs. the storage modulus $E''/E'$. Note that the dependence on the externally imposed curvature cancels (in this leading order theory). The nontrivial, finite $\omega$-solution then reads

$$\bar{\omega} = \sqrt{\frac{\bar{p}}{z_s} - 1} = \sqrt{\frac{\pi}{4} \frac{E'}{E''} \bar{p} - 1} \,, \qquad \text{(Supp. Eq.48)}$$

where we scaled the frequency and the thermal pumping by the thermal relaxation time scale, $\bar{\omega} = \omega\tau$ and $\bar{p} = p\tau$. This branch exists when the argument of the square root becomes positive, hence for $\bar{p} > \bar{p}_c = z_s = \frac{4}{\pi} \frac{E''}{E'}$ or

$$(\alpha_\parallel \Delta T_{\rm ext})_c \simeq \frac{l_{\rm th}}{R} \frac{E''}{E'} = \frac{k}{hR} \frac{E''}{E'} \,. \qquad \text{(Supp. Eq.49)}$$

The onset of motion is hence **supercritical** (i.e. continuous or second order) cf. Supplementary Fig. 13a), in agreement with the experiments [cf. Fig. 2D in the main manuscript].
The torque-velocity relation for a fiber ring can be also obtained from (Supp. Eq.45)-(Supp. Eq.47) by solving for $m_{\rm ext}$ and reads

$$m_{\rm ext} = \frac{\pi}{4} Y \frac{R^3}{R_{\rm ext}} \left( z_s - \frac{\bar{p}}{1 + \bar{\omega}^2} \right) \,. \qquad \text{(Supp. Eq.50)}$$

Note that the torque is proportional to the imposed curvature $m_{\rm ext} \propto \kappa_{\rm ext} = 1/R_{\rm ext}$, which hence also holds for the stalling torque.

**Fiber constrained to a spiral.** The description of a spiral with prescribed curvature is conceptually the same as for the closed circle, except that the the imposed curvature varies along the arc length [$\kappa_{\rm ext}(s) = 1/R_{\rm ext}(s)$], which makes a closed description difficult. As the curvature does not vary much for the spirals investigated in the main manuscript, in first order approximation one may use the description of a fiber closed to a circle, using the mean curvature of the spiral.

**Straight fiber.** In this case, one has to look for nontrivial solutions to the steady-state equations

$$-bxz = m_{\rm fric}(\omega) - m_{\rm ext}\,, \qquad \text{(Supp. Eq.51)}$$

$$0 = -\frac{x}{\tau} - \omega z\,, \qquad \text{(Supp. Eq.52)}$$

$$0 = p - \frac{z}{\tau} + \omega x\,. \qquad \text{(Supp. Eq.53)}$$

where we inserted the thermally induced curvature $\kappa_s = -\frac{x}{R}$, $b = B/R^2 = \frac{\pi}{4} Y R^2$ and the dissipative torque is given by $m_{\rm fric}(\omega = 0) = 0$ and $m_{\rm fric}(\omega \neq 0) = C_r \pi R^3 \bar{\rho} g$ for rolling friction. The trivial solution (for $m_{\rm ext} = 0$) is again given by $\omega = 0$, $x = 0$ and $z = p\tau$. As the torque balance is fulfilled identically, the open filament is torque free.
It is easy to show that for $m_{\rm ext} = 0$ nontrivial solutions exist if

$$\bar{\omega}^2 - \sqrt{\frac{b}{c}}\,\bar{p}\,\sqrt{\bar{\omega}} + 1 = 0\,, \qquad \text{(Supp. Eq.54)}$$

where we again scaled the frequency and the thermal pumping by the thermal relaxation time scale, $\bar{\omega} = \omega\tau$ and $\bar{p} = p\tau$. For sufficiently large drive (precisely for $\bar{p} > \bar{p}_c = \frac{4}{3} 3^{1/4} \sqrt{\frac{c}{b}} \simeq 1.755 \sqrt{\frac{c}{b}}$), two branches of finite $\omega$-solutions emerge, one stable and one unstable. The frequency at threshold is finite, $\bar{\omega}_c = \frac{1}{\sqrt{3}}$. Hence the onset of motion is subcritical (i.e. discontinuous or first order), cf. Supplementary Fig. 13b), again in agreement with the experiments [cf. Fig. 5B in the main manuscript]. The difference in the characteristics of the onset of rolling motion for a fiber closed in a circle (continuous) vs. a straight fiber (discontinuous) lies in the fact that in the former case, the symmetry is already broken by the externally imposed curvature, while in the latter this needs to be achieved via thermal curving.
We can conclude the following scalings for the self-propelled rolling motion, omitting numerical factors: the frequency at onset scales as

$$\omega_c \simeq \frac{D}{R^2}\,. \qquad \text{(Supp. Eq.55)}$$

One can show that for large driving the scaling is even $\omega_c \simeq \frac{1}{R^{7/3}}$. Note that this is stronger than the experimentally measured dependence of the frequencies (cf. Fig. 5D in the main manuscript) which yielded $\omega \simeq R^{-n}$ with $n = 0.75$. This discrepancy is due to the effect discussed above (see 'Linear and angular velocities'), i.e. deviations from the perfect fiber shape leading to slower angular velocities. For the effective thermal drive at onset we get $p_c = \frac{1}{\tau}\sqrt{\frac{c}{b}} = \frac{D}{R^2}\sqrt{\frac{\sigma_d}{Y}}$, where we introduced the dissipative stress associated with rolling friction, $\sigma_d = 4 C_r \rho g R$. For the thermal strain at onset we hence get

$$(\alpha_\parallel \Delta T_{\rm ext})_c \simeq \frac{l_{\rm th}}{R}\sqrt{\frac{\sigma_d}{Y}} = \frac{k}{hR}\sqrt{\frac{\sigma_d}{Y}}\,, \qquad \text{(Supp. Eq.56)}$$

with the heat conductivity $k = k_{\rm pol}$ and the heat transfer coefficient $h$.
Finally, one can solve (Supp. Eq.51)-(Supp. Eq.53) for the external torque to get the torque-velocity relation

$$m_{\rm ext} = c - b\bar{p}^2 \frac{\bar{\omega}}{(1+\bar{\omega}^2)^2}\,. \qquad \text{(Supp. Eq.57)}$$

This formula was used to fit the experimental data in Fig. 5C in the main manuscript, where fibers rolling on an inclined plane were studied.

### Energy storage in spirals

We will apply here the approximation just discussed that the spiral can be described by its mean curvature $\langle\kappa_{\rm ext}\rangle = 1/\langle R_{\rm ext}\rangle$. The angular velocity for free turning is then given by (Supp. Eq.48) as $\omega_{\rm fr} = \omega(m_{\rm ext} = 0) = \frac{1}{\tau}\sqrt{\frac{\bar{p}}{z_s} - 1}$ and for the stalling torque, $m_s$, one gets from the torque-velocity relation, (Supp. Eq.50),

$$m_s = m_{\rm ext}(\omega = 0) = \frac{\pi}{4} Y \frac{R^3}{\langle R_{\rm ext}\rangle} (z_s - \bar{p}) \propto \langle\kappa_{\rm ext}\rangle \,. \qquad \text{(Supp. Eq.58)}$$

We can immediately read off the scaling (for large thermal driving $\bar{p} \gg z_s$)

$$m_s \simeq Y R^3 \kappa_{\rm ext} \alpha_{\parallel} \Delta T_{\rm ext} \,, \qquad \text{(Supp. Eq.59)}$$

which for the total torque along the spiral, $M_s = L m_s$, yields the one given in the main manuscript. For simplicity we will approximate the torque-velocity relation by the straight line connecting $(\omega = 0, m_{\rm ext} = -m_s)$ to $(\omega = \omega_{\rm fr}, m_{\rm ext} = 0)$, i.e. we write

$$m_{\rm ext} = -m_s + \frac{\omega}{\omega_{\rm fr}} m_s \,. \qquad \text{(Supp. Eq.60)}$$

Let us now consider the spiral fiber motor as shown in Fig. 3A in the main manuscript. The inner end of the spiral is clamped, the outer end is free to move. In the confined spiral geometry, the thermally driven torque induces rotations along the local tangent, with the fiber accumulating twist all along the spiral path. We can interpret the approximate torque-velocity relation, (Supp. Eq.60), as an equation for the twist angle of the fiber, $\psi(s)$, with $s$ the arc length along the spiral path: we identify $\omega = \dot{\psi}$ and $m_{\rm ext} = C\psi''$, where $C = \gamma B = \gamma\frac{\pi}{4} Y R^4$ is the torsional stiffness, $\gamma = 1/(1+\nu)$ and $\nu$ Poisson's ratio. Rewriting then leads to

$$\dot{\psi} = D_\psi \psi'' + \omega_{\rm fr} \,, \qquad \text{(Supp. Eq.61)}$$

which has the form of a diffusion equation with a source term. The effective diffusion/stiffness reads $D_\psi = \frac{C\omega_{\rm fr}}{m_s} \propto \langle\kappa\rangle^{-1}$.
The general solution of (Supp. Eq.61) for the boundary conditions $\psi(0) = 0$ and $\psi'(L) = 0$ – corresponding to one fixed end and one free end, with $L$ the length of the fiber – and the initial condition $\psi(t = 0) = 0$ is given by

$$\psi(s,t) = \frac{2\omega_{\rm fr}}{L D_\psi} \sum_{n=0}^{\infty} \frac{\sin(k_n s)}{k_n^3} \left(1 - \exp\left(-D_\psi k_n^2 t\right)\right) \,, \qquad \text{(Supp. Eq.62)}$$

where $k_n = \frac{(2n+1)\pi}{2L}$. The fits to the experimental data [cf. inset of Fig. 3C in the main manuscript] show that a one-mode approximation, taking only the slowest mode $k_0 = \frac{\pi}{2L}$ into account,

$$\psi(s,t) = \frac{16 L^2 \omega_{\rm fr}}{\pi^3 D_\psi} \sin\left(\frac{\pi s}{2L}\right) \left(1 - \exp\left(-\frac{D_\psi \pi^2}{4L^2} t\right)\right) \,, \qquad \text{(Supp. Eq.63)}$$

is sufficient. For the number of turns we hence have

$$N(t) = \frac{\psi(L,t)}{2\pi} = \frac{8L^2\omega_{\mathrm{fr}}}{\pi^4 D_\psi}\left(1-\exp\left(-\frac{D_\psi\pi^2}{4L^2}t\right)\right), \qquad \text{(Supp. Eq.64)}$$

which was fitted to the data [cf. inset of Fig. 3C in the main manuscript] to get $D_\psi$ and $\omega_{\mathrm{fr}}$, and finally via $D_\psi = \frac{C\omega_{\mathrm{fr}}}{m_s}$ the total stalling force $M_s = Lm_s$ as displayed in Fig. 3D in the main manuscript.
For the stored energy [as shown in Fig. 3C in the main manuscript] one calculates

$$E = \frac{C}{2}\int_0^L \left(\psi'\right)^2 ds = \frac{16CL^3\omega_{\mathrm{fr}}^2}{\pi^4 D_\psi^2}\left(1-\exp\left(-\frac{D_\psi\pi^2}{4L^2}t\right)\right)^2. \qquad \text{(Supp. Eq.65)}$$

For $t\to\infty$ and large thermal driving, $\bar{p}\gg z_s$, using $D_\psi = \frac{C\omega_{\mathrm{fr}}}{m_s}$ and (Supp. Eq.59) we get the scaling

$$E \simeq \frac{CL^3\omega_{\mathrm{fr}}^2}{D_\psi^2} \simeq \frac{L^3}{YR^4}m_s^2 = Y\kappa_{\mathrm{ext}}^2\left(\alpha_\parallel\Delta T_{\mathrm{ext}}\right)^2 R^2L^3. \qquad \text{(Supp. Eq.66)}$$

Dividing by the fiber volume $V\simeq R^2L$ we get the scaling mentioned in the main manuscript.
Note that the formulas given here, although they fit the data very well, are only approximate due to the use of the mean curvature of the spiral and of the simplification of the torque-velocity relation.

## Supplementary figures

Supplementary figures 1 to 13.

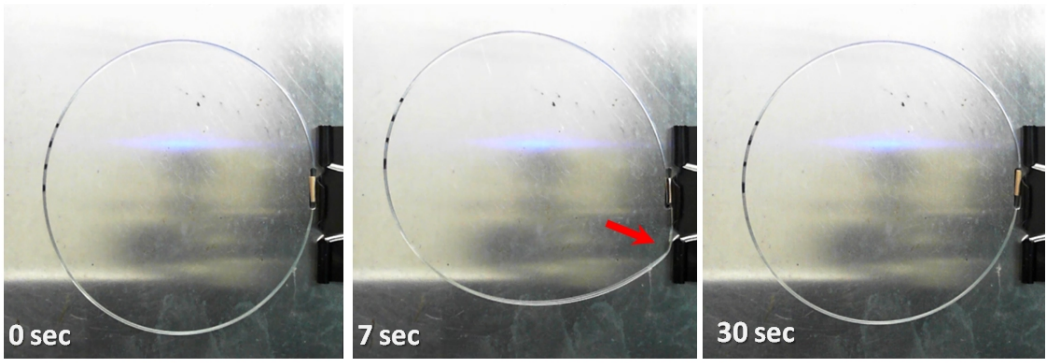


Supplementary Fig. 1: Collective spontaneous self-healing of defects in a circular fiber motor from nylon-6 rotating at 190°C. A strong deformation defect (kink) emerges at time $t = 7$ s and persists for several seconds. The continued collective rotation of the fiber leads to a complete self-healing at a later time ($t = 30$ s). See also supplementary video 6.

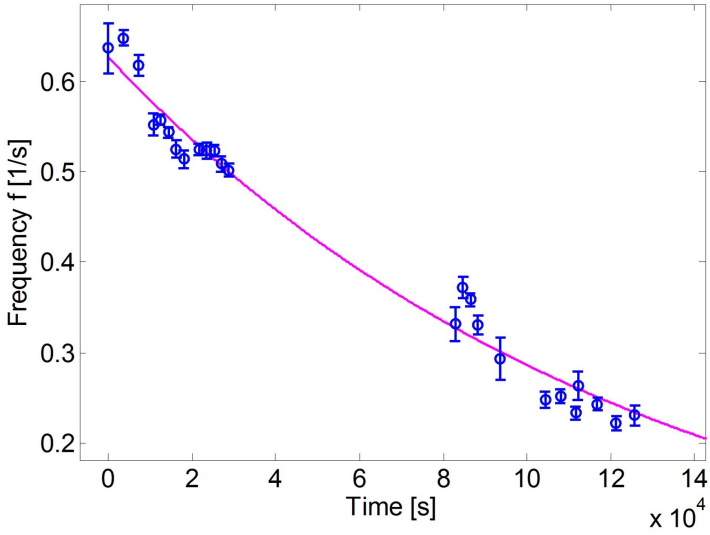


Supplementary Fig. 2: Continuous operation long time-testing of a spiral fiber motor. The fiber (nylon-6) is guided to a 13 turn, 0.6 mm diameter spiral and runs at T=160°C. The magenta line is a fit to $f(t) = f_0 \exp\left(-\frac{t}{t_r}\right)$, with $f_0 = 0.63$ Hz and with the exponential frequency relaxation time of $t_r = 34\,\mathrm{h}$ ($1.28 \times 10^5\,\mathrm{s}$).

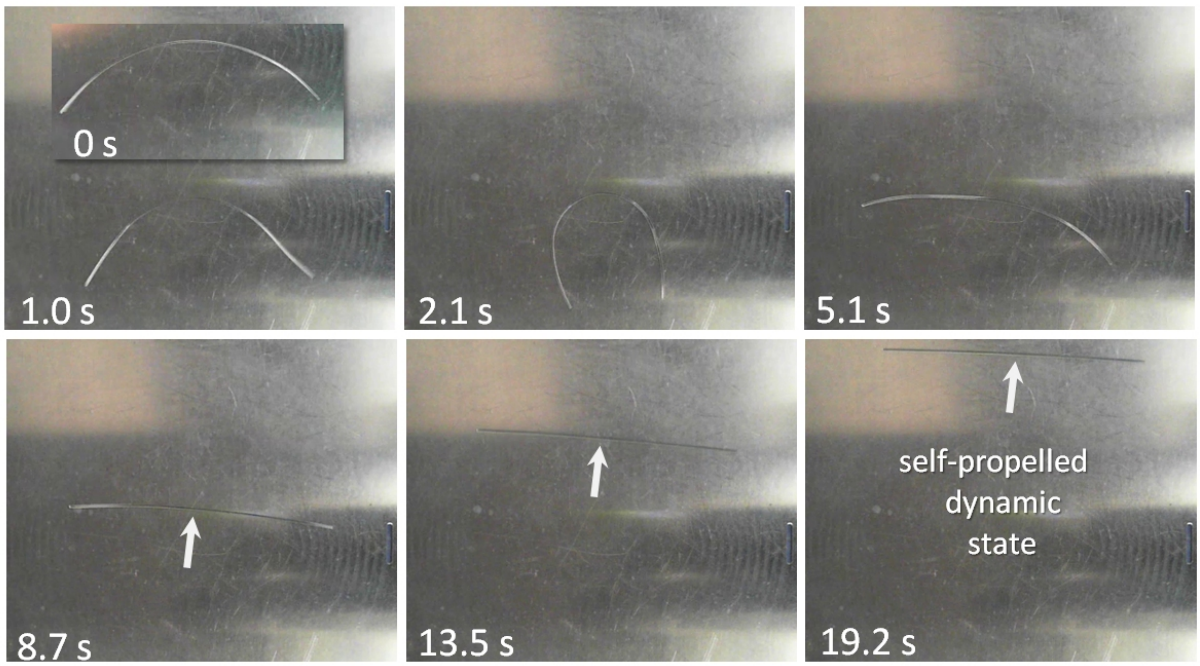


Supplementary Fig. 3: Slow annealing of a 800 $\mu$m nylon fiber at 110°C results in some transient reshaping and eventually within the time course of 10-20 seconds leads to an ideally straight and rolling fiber. See also supplementary video 4.

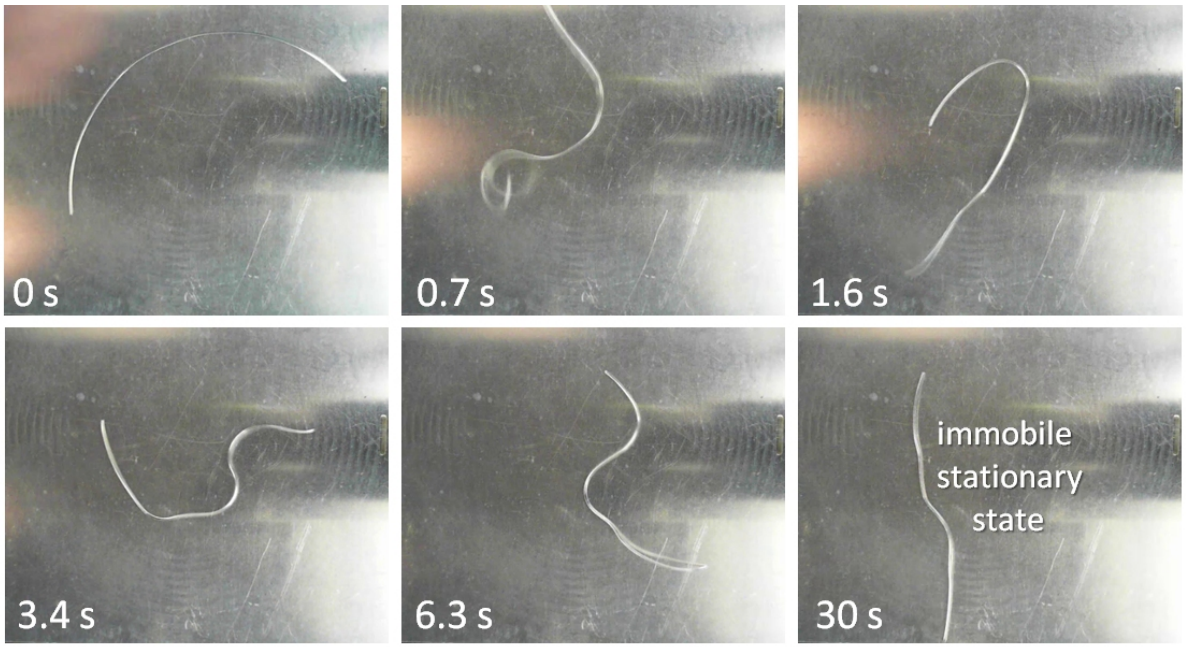


Supplementary Fig. 4: Exposing a nylon fiber (800 $\mu$m) directly to an elevated temperature (180°C) results in rapid uncontrolled reshaping. The final shape remains stationary and does not move or roll over the surface. See also supplementary video 4.

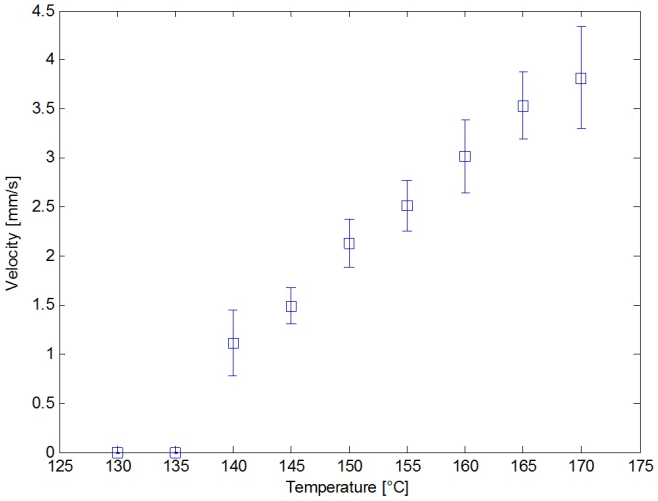


Supplementary Fig. 5: Rolling velocity as a function of the plate temperature for PVDF fibers of diameter 0.5 mm.

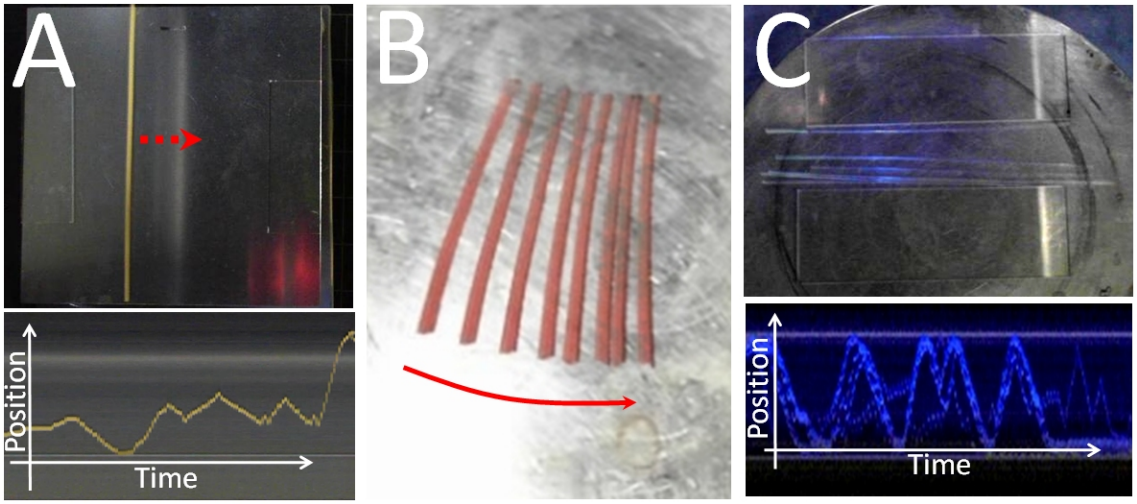


Supplementary Fig. 6: a) Dried starch rods (spaghetti) propelled on a heating plate. The lower panel shows a kymograph (space-time plot) of the motion orthogonal to the fiber axis. b) Silicone rubber rod, superposition of images. The rolling trajectory is slightly curved due to the slight conical shape of the sample. c) Collective motion of several nylon-6 rods confined between two spacers. The lower panel again shows the kymograph. See also supplementary video 3.

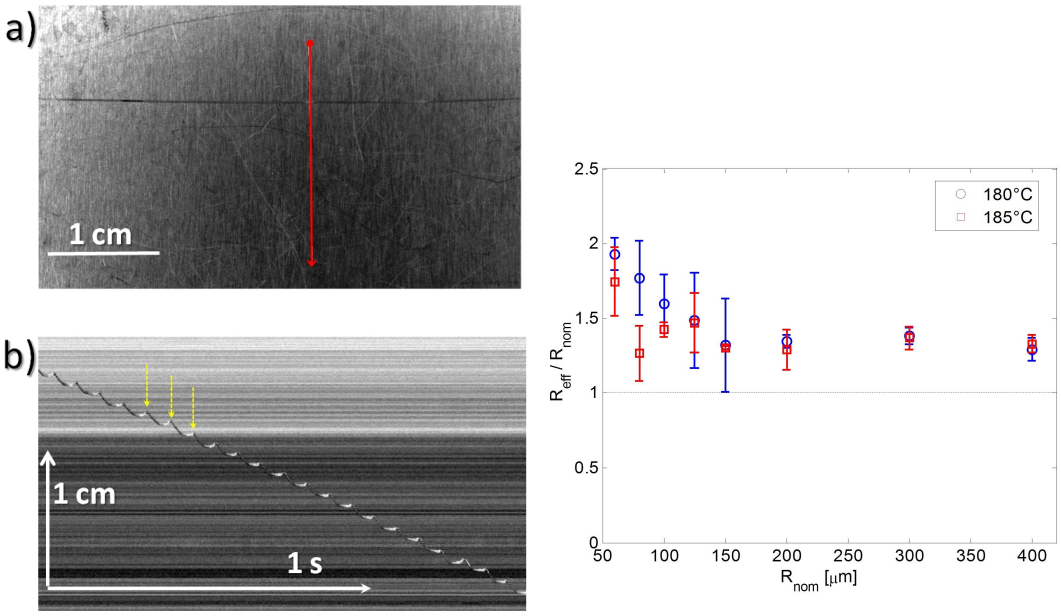


Supplementary Fig. 7: Measurement of linear and angular velocity. a) A nylon-6 fiber of radius 60 $\mu$m rolling at 185°C. b) Line-scan along the red line in a). In addition to a constant velocity linear motion, the fiber displays a velocity modulation (yellow arrows) in phase with its rotary motion. On the right, the effective radius of the fiber is shown, deduced from the ratio of linear and angular velocity.

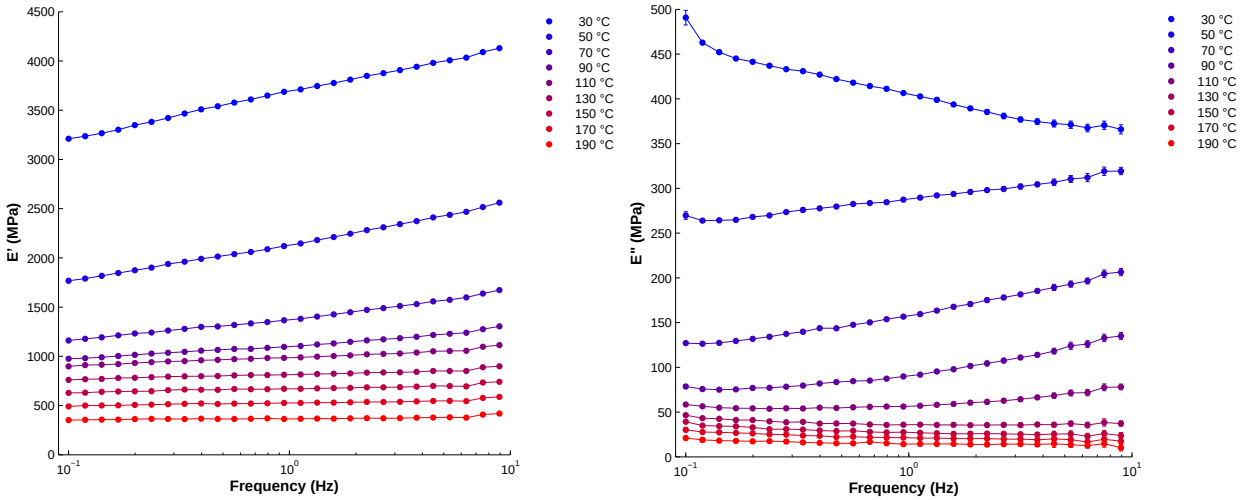


Supplementary Fig. 8: Mechanical characterization of nylon-6 fibers. Left: The storage modulus vs. frequency for temperatures from 30 to 190°C. Right: The loss modulus vs. frequency for the same temperature range.

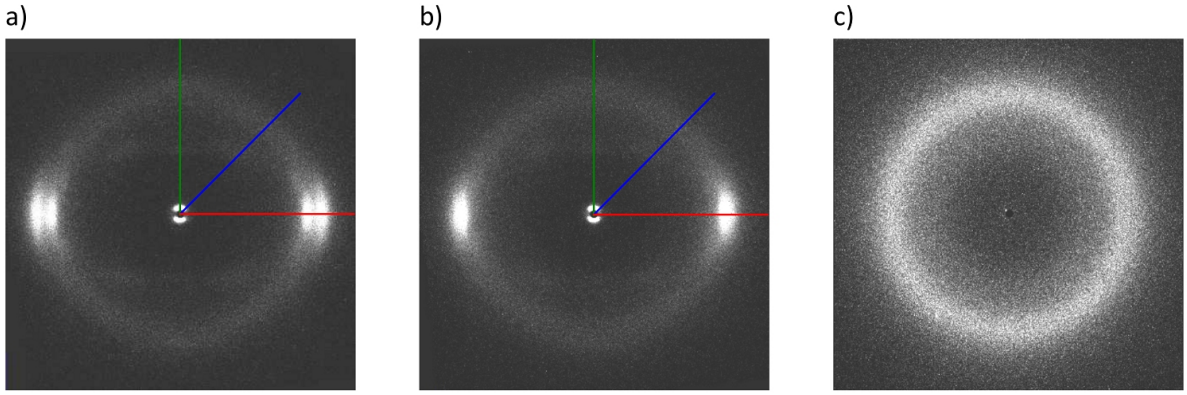


Supplementary Fig. 9: 2D WAXS intensity profile for the annealed nylon-6 fiber at a) 120°C, b) 185°C, and c) 240°C showing the anisotropy of the signals before melting above 220°C. Note: The fiber axis lies in the vertical direction.

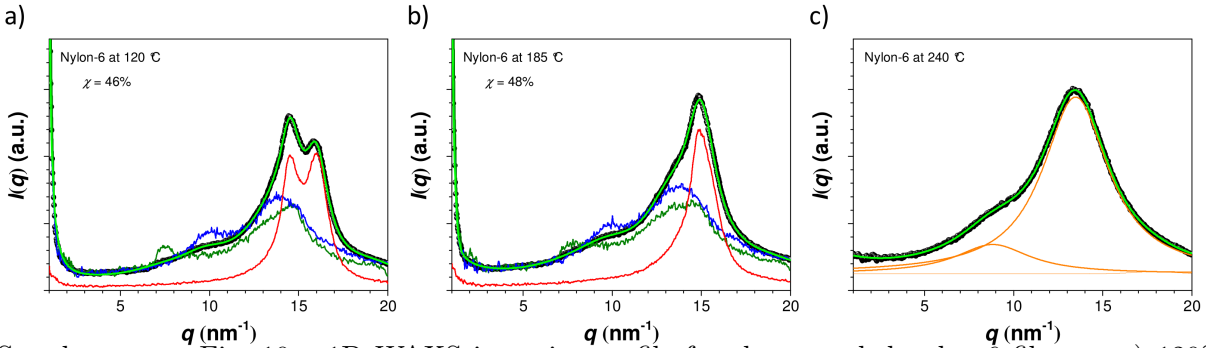


Supplementary Fig. 10: 1D WAXS intensity profile for the annealed nylon-6 fiber at a) 120°C, b) 185°C, and c) 240°C and the corresponding fitting curve (light green curve). The red (equatorial), blue (45 degrees oblique) and dark green (meridional) curves correspond to the scattering profiles from the sections in Supplementary Fig. 9. The orange curves in c) are the amorphous peaks contributing to the signal for the polymer melt.

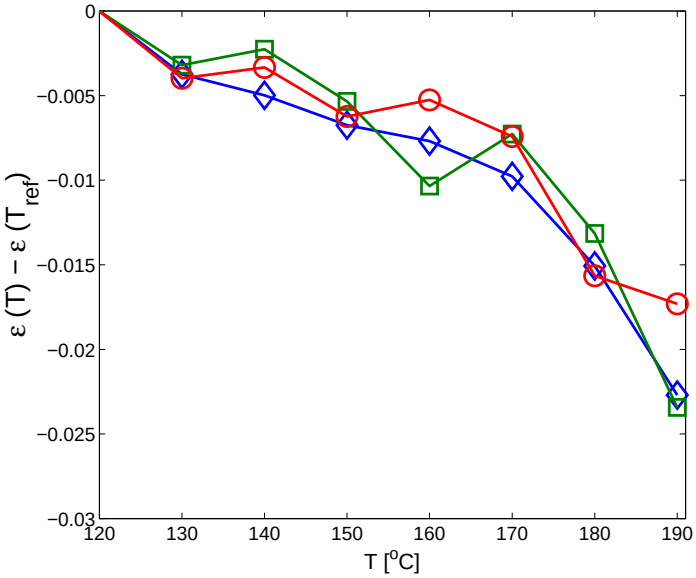


Supplementary Fig. 11: Relative longitudinal strain of rolling fiber samples with diameters 0.6 mm and lengths between 10 and 12 cm.

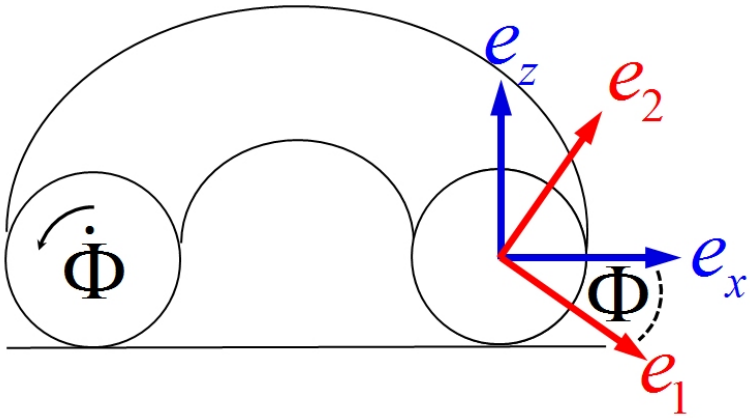


Supplementary Fig. 12: Sketch of the geometry. Shown is a fiber that is confined in the $X$-$Y$-plane (by its own weight). When we consider a cross-section (in the $X$-$Z$-plane), we can assume without restriction that the curvature is along $X$. The co-rotating frame is spanned by the vectors $e_1$ and $e_2$, with the angle $\Phi$ between $e_1$ and $e_x$.

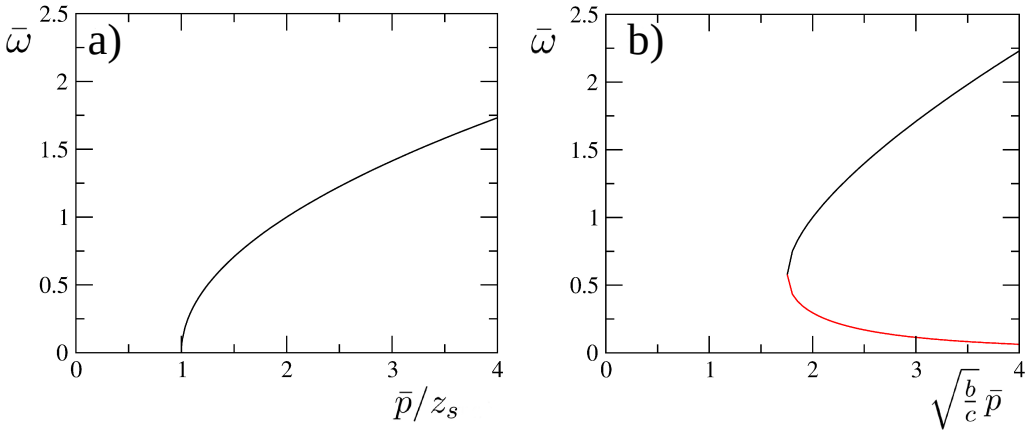


Supplementary Fig. 13: a) Continuous onset of rotation of a fiber closed to a ring as given by (Supp. Eq.48). Shown is the scaled angular velocity, $\bar{\omega}$, as a function of rescaled effective driving $\bar{p}/z_s$. b) Discontinuous onset of rolling motion for a straight fiber as given by (Supp. Eq.54). Shown is the scaled angular velocity, $\bar{\omega}$, as a function of rescaled effective driving, $\sqrt{\frac{b}{c}}\,\bar{p}$. The black branch is stable, the red one unstable.

## Supplementary References


[31] C. Millot, L. Fillot, O. Lame, P. Sotta, R. Seguela, *J. Therm. Anal. Calorim.* **122**, 307 (2015).

[32] Y. Katoh, M. Okamoto, *Polymer* **50**, 4718 (2009).

[33] K. Miyasaka, K. Makishima, *J. Polym. Sci. A* **5**, 3017 (1967).

[34] T. Itoh, *Jpn. J. Appl. Phys.* **15**, 2295 (1976).

[35] G. Gururajan, S. Sullivan, T. Beebe, D. Chase, J. Rabolt, *Nanoscale* **3**, 3300 (2011).

[36] M. Born, E. Wolf, *Principles of optics, 7th edition* (Cambridge University Press, Cambridge, 2002).